Rheological transition during large strain deformation of melting and crystallizing metapelites

Santanu Misra, Jean-Pierre Burg, Jean-Louis Vigneresse, David Mainprice

AGU PUBLICATIONS

JGR

Journal of Geophysical Research: Solid Earth

RESEARCH ARTICLE
10.1002/2013JB010777

Key Points:
- Large strain syn-tectonic partial melting and crystallization
- Rheological transition from strain rate sensitive to insensitive flow
- Fate of sediments dragged from accretionary wedge along subducting interface

Correspondence to:
S. Misra,
santanu.misra@erdw.ethz.ch

Citation:
Misra, S., J.-P. Burg, J.-L. Vigneresse, and D. Mainprice (2014), Rheological transition during large strain deformation of melting and crystallizing metapelites, *J. Geophys. Res. Solid Earth*, *119*, 3971–3985, doi:10.1002/2013JB010777.

Received 16 OCT 2013
Accepted 26 MAR 2014
Accepted article online 30 MAR 2014
Published online 1 MAY 2014

Rheological transition during large strain deformation of melting and crystallizing metapelites

Santanu Misra[1,2], Jean-Pierre Burg[1], Jean-Louis Vigneresse[3], and David Mainprice[4]

[1]Geological Institute, ETH, Zurich, Switzerland, [2]Institute of Geological and Nuclear Sciences, Wellington, New Zealand, [3]Université de Lorraine, Géoressources, UMR 7359, 54501, Vandoeuvre-lès-Nancy, France, [4]Géosciences Montpellier, CNRS UMR 5243, Université Montpellier 2, Montpellier, France

Abstract Torsion experiments ($\dot{\gamma}=3\times10^{-4}\,s^{-1}$) were performed to investigate the large strain ($\gamma_{max}=15$) rheology on quartz-muscovite aggregate as analogue to pelitic rocks undergoing melting and crystallization during deformation at 300 MPa confining pressure and 750°C temperature. Microstructures reveal four distinct but gradational stages of crystal-melt interactions during deformation—(a) solid state deformation, (b) initiation and domination of partial melting, (c) simultaneous partial melting and crystallization, and (d) domination of crystallization. The microstructural stages are linked to the rheology of the deforming samples. Partial melting starts at relatively low finite shear strains ($\gamma=1$–3) showing approximately 60% strain softening. At $\gamma=4$–10 the partially molten bulk material shows a steady state flow at low stress. Further crystallization of new crystals at the expense of melt between $\gamma=10$ and 15 causes weak strain hardening until the material fails by developing brittle fractures. The stress exponent (n), calculated at $\gamma=1$, 5, and 10, increases from ~3 to ~43, indicating a transition from power to power law breakdown or exponential flow of the bulk system. Hydrostatic experiments for equivalent times and conditions of the torsion experiments were also conducted to evaluate the reaction kinetics and microstructures under static conditions. The new experimental data establish that partially molten rock does not flow according to a constant strain rate-dependent power law (steady state) rheology. The rheological transition from strain rate sensitive to strain rate insensitive flow is interpreted as a function of melt-crystal ratio, their mutual interactions, and the evolution of microstructures in the partially molten rock.

1. Introduction

Partial melting of crustal rocks in natural conditions occurs when sufficient temperature and, to a less extent, pressure conditions are reached [*Lambert et al.*, 1969; *Thompson*, 1982; *Clemens and Vielzeuf*, 1987; *Vielzeuf and Holloway*, 1988]. This is independent of the ambient differential or deviatoric stress regime. In natural settings, the melting rock mass may be in a relatively stable state and essentially experiences the effects of hydrostatic pressure and temperature. Alternatively, in orogenic systems, the production of melt can occur while the rock mass deforms in response to differential stress. In any case, the amount, distribution, and flow of the melt may vary both spatially and temporally depending on the rock composition, the ambient pressure-temperature, the deformation rate, the amount of finite strain, and other physical factors such as pore fluid pressure [*Sawyer*, 1987; *Brown*, 1994; *Misra et al.*, 2011]. An additional factor is time through reaction kinetics, when minerals crystallize from parent solid crystals and/or nuclei in the partial melt.

The last few decades have witnessed the development of a significant knowledge of *rheology and dynamics of partially molten rocks*. Studies have covered a wide range of rock-melt systems documented at different space and timescales from field, experimental, and theoretical investigations. The bulk viscosity and rheology of two-phase systems, consisting of solid grains suspended within a fluid, has been derived by *Einstein* [1906] and *Roscoe* [1952]. Their equations have been employed to describe the rheology of partially molten rocks [*Van der Molen and Paterson*, 1979] and were one of the fundamental concepts behind that of *Rheological Critical Melt Percentage* (RCMP) [*Arzi*, 1978]. However, such interpretations do not consider strain partitioning between the phases [*Vigneresse and Tikoff*, 1999]. The application of RCMP coupled with percolation of melt theories [e.g., *Stauffer*, 1985; *Vigneresse et al.*, 1996] is more difficult when the melt content decreases while the volume fraction of new crystal increases and forms an interlocking network of solid grains that trap the melt as the rock permeability is reduced. *Vigneresse et al.* [1996] and *Burg and Vigneresse* [2002] have argued

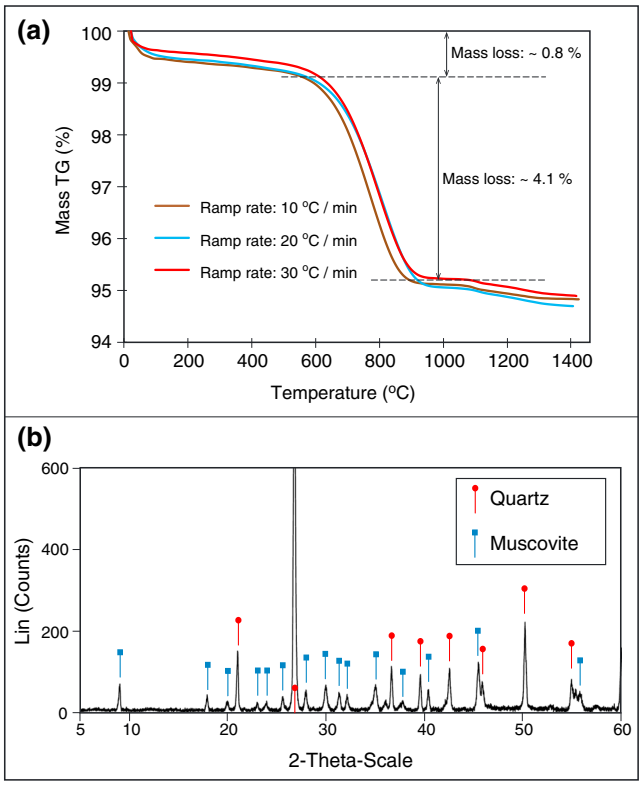

Figure 1. (a) Dehydration curves of muscovite used in this study. The data were obtained by a simultaneous thermogravimetry-differential scanning calorimetry (NETZSCH STA 409 C/CD) instrument installed in ETH Zurich. The tests were conducted in an inert Argon gas environment within a temperature range from room (14°C) to 1400°C at three different temperature ramps (10, 20, and 30°C). The data show that the rate and magnitude of dehydration of muscovite are independent of temperature ramping rate. A major and significant amount of mass loss (~4.12%) occurs from 500 to 900°C. This temperature range of maximum dehydration justifies the temperature condition (750°C) of the deformation and hydrostatic experiments presented in this study. (b) XRD analysis of the starting material after Hot Isostatic Press (HIP). The characteristic peaks of the X-ray intensity define only quartz and muscovite. This proves that the starting material did not undergo chemical reactions during the HIP.

that four domains explain the transitional behavior from solid to melt during progressive melting (geological anatexis) and melt to solid during magma crystallization. These domains are separated by thresholds; two control the response of melting rocks: (1) the *liquid percolation threshold*, at about 8% of melt, when individual melt pockets begin to connect and (2) the melt *escape threshold* at 20–25% melt when the melt may segregate and migrate in and out of the system. The other two thresholds control the behavior of crystallizing rocks: (3) the *rigid percolation threshold* at 55% of crystals corresponds to the formation of a rigid framework that can accumulate stress while the melt can still flow and (4) the *particle-locking threshold* at about 72–75% solid, when the system becomes locked. These studies further suggest that the transitions from solid to melt through partial melting and the reverse through crystallization are not symmetric and identical. However, a physical characterization of these thresholds is missing owing to the lack of experimental data from high finite strain experiments on polymineralic rocks.

Another line of study focused on the nature of the flow law of partially molten rocks undergoing deformation. These studies extrapolated deformation mechanisms and flow laws to natural strain rates, which are several orders of magnitude lower than laboratory strain rates. Earlier experiments on polymineralic rocks either in presence or in absence of partial melt concluded that aggregate rheology mainly obeys a power law for steady state creep with a calculated stress exponent (n) ranging from 1 to 7 [e.g., *Rutter and Neumann*, 1995; *Zimmerman and Kohlstedt*, 2004; *Rutter et al.*, 2006]. The flow mechanism, however, changes when solid particles interact with the fluid phase, and the amount and packing of solid phases continuously affect the relative viscosity of the bulk system [*Jinescu*, 1974]. *Sherby et al.* [1954], *Sherby* [1962], and *Carter and Tsenn* [1987] predicted that in certain physical conditions and at high shear strains the n values are much higher and an exponential dependence of strain rate on stress best describes the flow law. Following this argument, the steady state flow laws break down when other deformation mechanisms and rheologies, such as microplasticity, semibrittle deformation, and cataclastic flow, dominate.

Partial melting and subsequent recrystallization of crustal rocks are generally attributed to regional metamorphism [*Sawyer*, 1994; *Brown and Solar*, 1997; *Kalt et al.*, 1999; *Brown*, 2007]. However, this geological evidence mainly stems from petrological studies (e.g., pressure and temperature conditions), which rarely discuss the role of deformation. A more complete investigation demands considering finite strain. Dynamic interactions between solid and fluid phases involve strain partitioning (because of rheological contrast and shear localization) and rate of melting and crystallization, which govern the bulk behavior of the

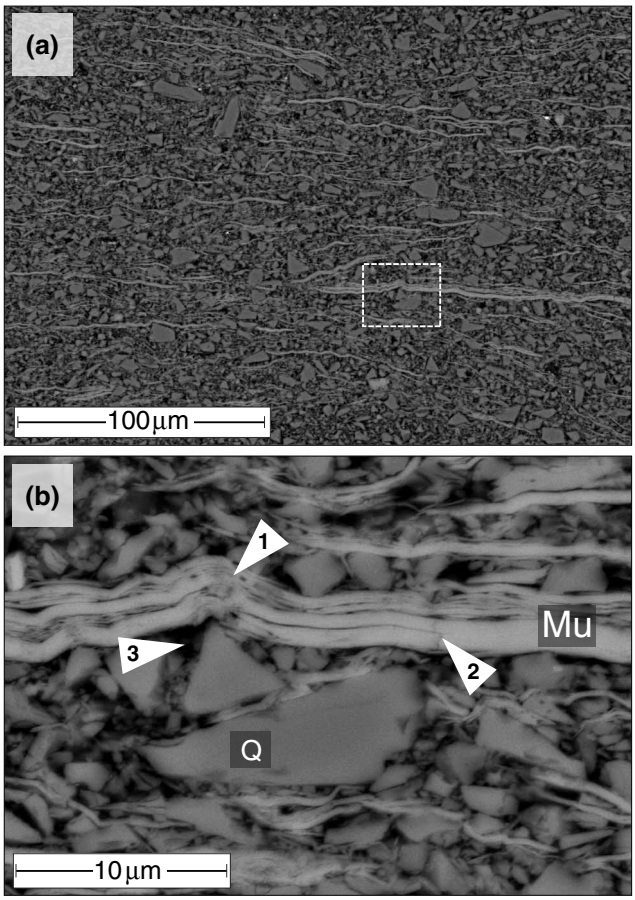

Figure 2. Microstructure of the starting material consisting of quartz (Q) and muscovite (Mu) in SEM under BSE mode. The observed plane is parallel to the UCP direction. (a) The flaky muscovite grains aligned subperpendicular to the UCP direction defines crude foliation. (b) A zoomed in view of the stippled rectangular area from Figure 2a showing the disposition of muscovite (Mu) and quartz (Q). Note microbuckling, kinking (arrowhead 1), and microfracture (arrowhead 2) in the muscovite grains. Arrowhead 3 marks one of the intergrain pore spaces.

solid-fluid system during its transitional stages [*Barboza and Bergantz*, 1998; *Renner et al.*, 2000; *Burg and Vigneresse*, 2002; *Misra et al.*, 2011].

To investigate the role of incremental finite strain on the partial melting and subsequent crystallization in metapelites, a series of laboratory experiments on dry, synthetic quartz-muscovite aggregates were conducted. Samples were deformed up to finite shear strains of approximately 15. The experimental confining pressure and temperature were kept constant. Calculation of stress exponent (n) derived from stepping strain rate (SSR) experiments revealed the flow properties of the bulk system at different values of finite shear strains. This work also includes and enlarges experimental data from *Misra et al.* [2011] and *Tumarkina et al.* [2011].

2. Experimental Materials and Methods

2.1. Fabrication of Starting Material

We used a dry mixture of quartz and muscovite as a simplified analogue for pelite. Pure and fine-grained quartz and muscovite were received from Alberto Luisoni, Switzerland (www.albertoluisoni.ch), and used to fabricate the starting material. Thermogravimetric analysis of muscovite showed that the dehydration of muscovite is independent of ramping rate of temperature (10, 20, and 30°C/min), and it occurs in two major stages. About 0.76% mass loss at room temperature (14°C) to 500°C and 4.12% mass loss from approximately 500 to 900°C (Figure 1a). The preparation of the synthetic starting samples (first, cold pressed at 200 MPa and then hot pressed at hydrostatic pressure of 160 MPa and temperature of 580°C for 24 h) was described in [*Misra et al.*, 2011].

X-ray diffraction (XRD) analysis of the synthesized solid material showed that quartz and muscovite had not reacted and retained their original composition during preparation (Figure 1b). The samples have porosity of about 12–15%. Flat surfaces of the cylindrical samples, parallel to the Uniaxial Cold Press (UCP) direction, were cut and polished to observe the initial microstructures under scanning electron microscope (SEM) in backscattered electron (BSE) mode. The microstructure consisted of a planar fabric defined by the basal planes (001) of muscovite grains oriented subperpendicular to the UCP direction (Figure 2a). Quartz grains were mostly located between the planar fabric elements with muscovite locally wrapping quartz grains. Bending and kinking of platy muscovite grains in response to UCP were also observed in places (Figure 2b). Open pores mostly occurred at the contact of straight quartz grain edges and flat basal planes of muscovite grains (Figure 2b).

2.2. Deformation Assembly and Apparatus

Deformation experiments were performed in an internally heated high pressure-temperature apparatus equipped with a torsion actuator [*Paterson and Olgaard*, 2000]. The cylindrical sample was placed between two thin (3 mm) alumina spacers of 10 mm diameter and then sandwiched by two sets of solid alumina and

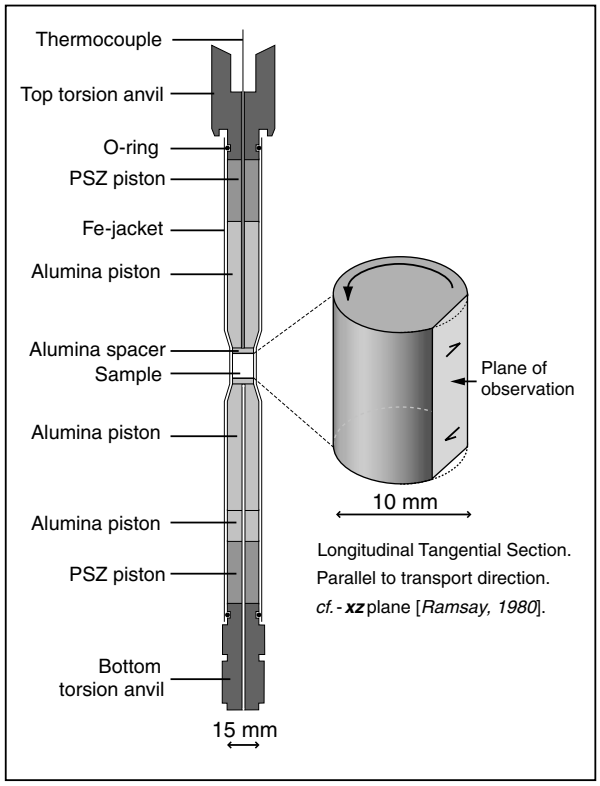

Figure 3. A schematic illustration of sample assemblies for torsion and hydrostatic experiments in Paterson-type deformation apparatus. In the right, a sketch of the deformed sample shows the plane of observation (longitudinal tangential section) for microstructural analysis.

partially stable zirconia pistons of 15 mm diameter (Figure 3). These pistons reduce heat conduction away from the sample and provide a stable precalibrated flat thermal profile along the sample length. The whole assembly was inserted into an iron tube with 15 mm inner diameter and 0.25 mm wall thickness to isolate the specimen from the pure Argon gas used as the confining medium. The iron jacket has been swaged down in the central part where the sample and two adjacent alumina discs have 10 mm diameter (Figure 3). Passive straight scratches were drawn along the long axis of the iron tube to visualize the shear strain. Torsion anvils were added with O-rings against the jacket to seal both ends of sample assembly from the confining gas. The whole assembly was inserted vertically into the deformation apparatus.

2.3. Experiments and Postprocessing

Constant displacement rate experiments corresponding to a constant imposed shear strain rate ($\dot{\gamma} = 3 \times 10^{-4}\,s^{-1}$) were performed at 300 MPa confining pressure and 750°C temperature for a series of finite shear strains (γ) from 0.5 to 15.0. Confining pressure was monitored with a pressure gauge (resolution 1 MPa; fluctuation ± 4 MPa). Temperature was measured with a K-type thermocouple (placed 3 mm from the top of the sample, Figure 3), with resolution of 1°C and fluctuations ± 2°C. The torque (M) was measured in N m with different pairs of Linear Variable Differential Transformers placed in the internal load cell (resolution 0.1 N m). A Rotational Variable Displacement Transformer was placed at the top of the torsion gearbox, which was mechanically connected to the top specimen anvil to measure the angular displacement (θ) in radians for an applied constant angular displacement rate ($\dot{\theta}$ in rad/s). For a given length (l) and radius (r) of the sample, θ with shear strain (γ) and $\dot{\theta}$ with shear strain rate ($\dot{\gamma}$) are related to each other by the equations $\theta = \frac{1}{r}\gamma$ and $\dot{\theta} = \frac{l}{r}\dot{\gamma}$, respectively. The vessel was initially pressurized up to 240 MPa. Then it increased toward the target confining pressure due to the temperature increase using a ramp of 15°C/min. The confining pressure was adjusted (300 MPa) either by pumping or releasing argon gas after reaching the target temperature of 750°C. After the experiment, both confining pressure and temperature were reduced quickly to room temperature (60°C/min) and pressure in order to avoid any static crystal growth and to retain the deformation-induced microstructure. Two other sets of experiments were performed to complement torsion experiments. Stepping strain rate (SSR) experiments were conducted at 750°C and 300 MPa to calculate the stress exponent (n) values and define the bulk rheology of samples after reaching three finite shear strains ($\gamma = 1$, 5, and 10). In addition, a series of hydrostatic experiments (i.e., with no differential stress) were carried out at 750°C and 300 MPa for 1, 2, 5, 10, and 15 h to compare microstructures of deformed and undeformed samples and their crystal-melt proportions.

All samples, except the SSR ones, were observed in longitudinal tangential section (Figure 3). This section is perpendicular to the initial planar fabric. Polished surfaces and thin sections were prepared to observe and analyze the samples with the SEM. In the deformed samples, the direction of bulk shear stress is approximately parallel to the section plane. This plane equates the *XZ* plane of finite strain ellipsoid in a natural shear zone [e.g., *Ramsay*, 1980].

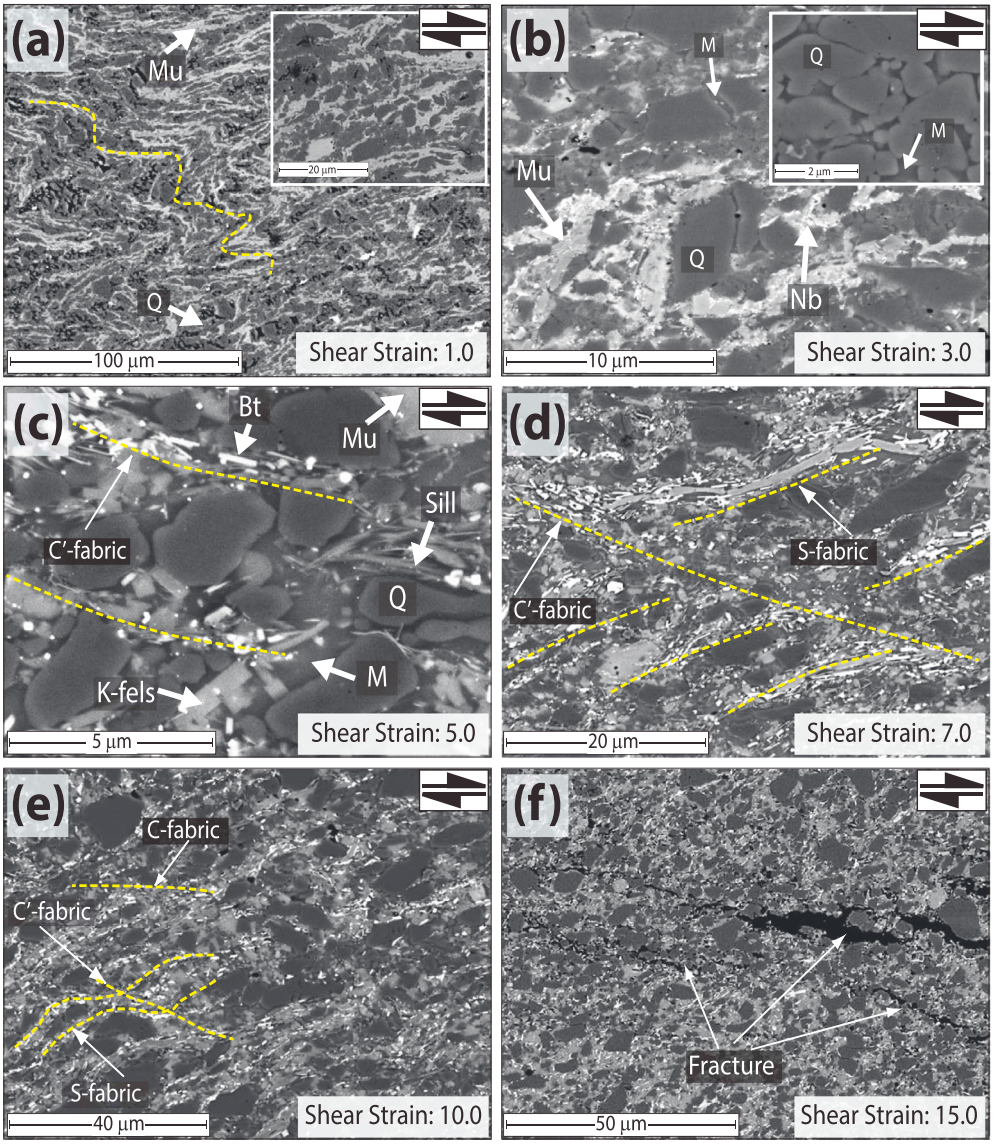

Figure 4. Evolution of microstructures in response to partial melting and subsequent crystallization with progressive shearing of quartz-muscovite samples. The deformed samples were cut and polished (Figure 3) to observe under SEM with BSE mode. The widths of the microphotographs are different to reveal the characteristic microstructures at different stages of deformation. The dotted yellow lines highlight shear-induced deformation features. See text for descriptions. Abbreviations—Q: quartz, Mu: muscovite, M: melt, Nb: neoblasts, K-fels: K-feldspar, Bt: biotite, and Sill: sillimanite.

3. Results

3.1. Evolution of Microstructure in Torsion and Hydrostatic Experiments

Microstructural descriptions of SEM images and chemical analyses of deformed samples (initially consisting of 70% quartz and 30% muscovite) at various strain levels have been reported by *Misra et al.* [2011] and *Tumarkina et al.* [2011]. These studies have shown that melt was generated and that new minerals (K-feldspar, biotite, sillimanite, and accessory spinel) crystallized from the melt. Without repeating these observations, this section mostly focuses on describing the deformation-induced microstructures relevant for interpreting the rheological data.

The microstructures evolved with progressive deformation in response to both the imposed bulk shear strain and chemical reactions between muscovite and quartz. Some samples had to be unloaded before starting deformation, after nearly achieving the target pressure-temperature because of either leaking (jacket failure) or other technical problems. These samples were studied to measure porosity and compaction. The initial

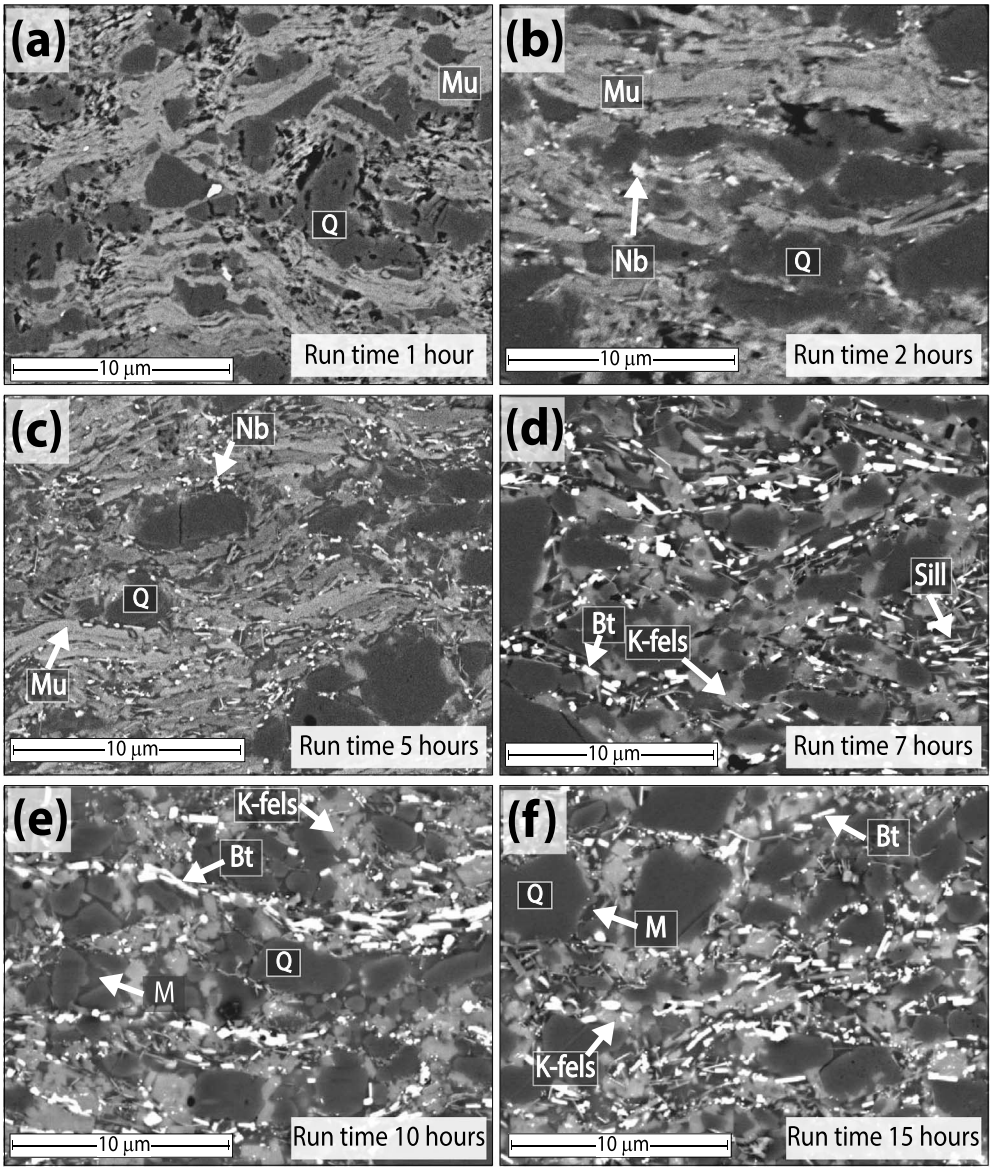

Figure 5. Microstructures of the hydrostatic experiments as function of run time showing partial melting and crystallization of quartz-muscovite samples. Samples were cut at the outer boundary (longitudinal tangential section) and polished to observe under SEM with BSE mode. See text for descriptions. Abbreviations—Q: quartz, Mu: muscovite, M: melt, Nb: neoblasts, K-fels: K-feldspar, Bt: biotite, and Sill: sillimanite.

porosity (12–15%) decreased to approximately 5% on reaching 300 MPa and 750°C. Pores were mostly between quartz grains. The porosity of samples was reduced to 1–2% by low shear strains ($\gamma = 0.5–1.0$). Local kinking and disharmonic, asymmetric bending and folding of muscovite grains were observed (Figure 4a). Muscovite and quartz grains rotated in response to shear so that their long axes became approximately parallel to the bulk extension direction (Figure 4a, inset). Because of the shear-induced passive rotation, muscovite grains became stretched and boudinaged along the principal extension direction. A small amount of melt was generated along grain boundaries and junctions between quartz and muscovite grains at $\gamma = 2.5–3.0$. Melt was associated with few new, nanometer-sized crystals with very high backscatter coefficient concentrated along the grain boundaries (Figure 4b and inset). The overall microstructure featured these new reaction products (neoblasts) and old-rounded quartz and relicts of muscovite grains (Figure 4b). At higher shear strains ($\gamma = 5.0–7.0$), the sample showed minor shear localization along C′ orientation and rough S-C′ fabric [*Berthé et al.*, 1979]. The fabric was defined by the concentration of oriented biotite and sillimanite crystals

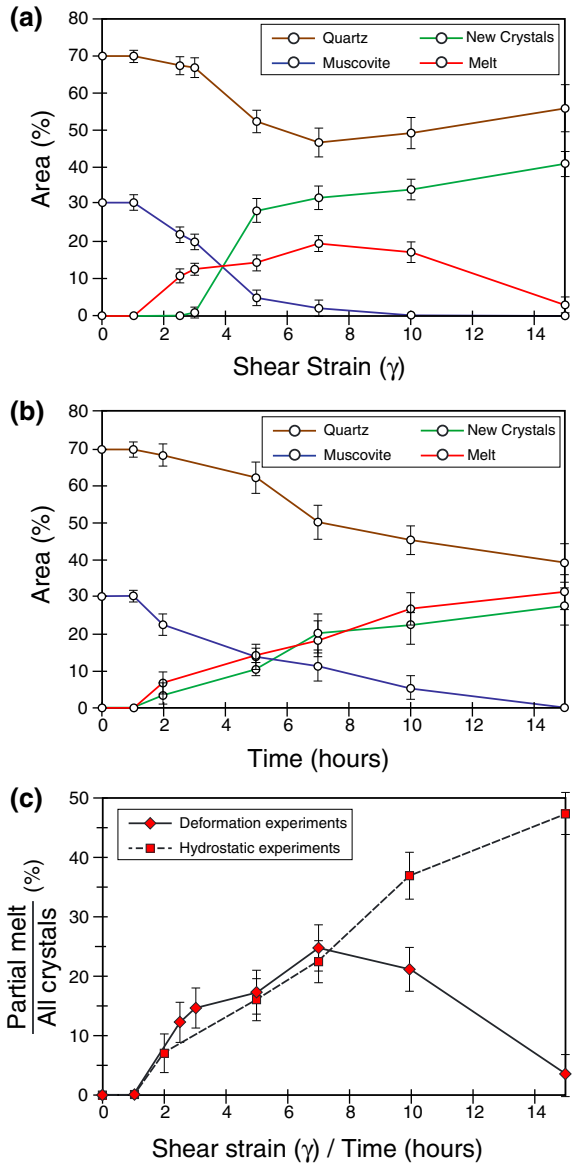

Figure 6. Average area percentage of quartz, muscovite, new crystals, and melt in (a) deformation (torsion) and (b) hydrostatic experiments plotted against shear strain and time, respectively. (c) A comparative plot of partial melt to total crystal ratio in deformation and hydrostatic experiments.

along narrow melt channels (Figures 4c and 4d). Quartz grains were parallel to the maximum stretching direction. Further deformation ($\gamma \sim 10.0$) showed extensive crystallization of K-feldspar. Most of the K-feldspar grains were typically euhedral and rectangular though subhedral to anhedral grains occur (Figure 4e; also see Figure 4c). At this strain level ($\gamma \sim 10.0$) muscovite grains were completely consumed, and quartz grains with rounded and smooth boundaries were present. The new crystals like K-feldspar, sillimanite, and biotite had occupied the patchy melt pockets already present in lower shear strain samples. A shear-induced S fabric [*Berthé et al.*, 1979] was defined by dark gray quartz, crystallized lighter gray, and white new minerals and partial melt (Figure 4e). In addition to the C′ fabrics, bulk shear parallel, weakly developed C fabrics were defined by narrow melt channels with systematic subparallel alignment of sillimanite and K-feldspar crystals (Figure 4e). Samples sheared up to $\gamma \sim 15.0$ were devoid of melt and were characterized by relict quartz grains homogeneously distributed in the matrix of K-feldspar and biotite (Figure 4f). The sample surface showed numerous tensile and shear microcracks forming an en echelon array at 20–45° to the bulk shear direction (Figure 4f). Some fractures showed an overall sigmoidal geometry.

Hydrostatic experiment conducted for 1 h retained the initial microstructure and did not show any sign of partial melting or new crystallization (Figure 5a). After 2–5 h, tiny melt pockets (approximately 7–12%) with small new crystals (approximately 3–9%) had occurred along grain boundaries (Figures 5b and 5c). Melt and new crystal content (approximately 12–27% melt and 9–20% crystals, respectively) increased at 5–10 h hydrostatic condition (Figures 5d and 5e). Melt was present in both isolated pockets and as continuous films along grain boundaries. Most of the muscovite grains were replaced by arrays of biotite, sillimanite, and K-feldspar along the planar fabric inherited from hot pressing (Figure 5e). At 15 h both the melt and new crystal content had increased to approximately 30% and 28%, respectively, at the expense of quartz and muscovite (Figure 5f).

3.2. Melt-Crystal Ratio in Torsion and Hydrostatic Experiments

Area fractions of partial melt and new crystals were measured from SEM images recorded in backscattered electron (BSE) mode. Details of the measurement techniques are described in *Misra et al.* [2011]. The data are presented in percent area of quartz, muscovite, melt, and new crystals (K-feldspars + biotite + sillimanite + spinel) as a function of shear strain and time for deformation and hydrostatic experiments, respectively (Figures 6a and 6b). It may be noted that given the constant strain rate ($\dot{\gamma} = 3 \times 10^{-4}\,s^{-1}$) and the sample geometry (10 mm diameter), it takes approximately 1 h (0.93 h) to achieve one magnitude of finite

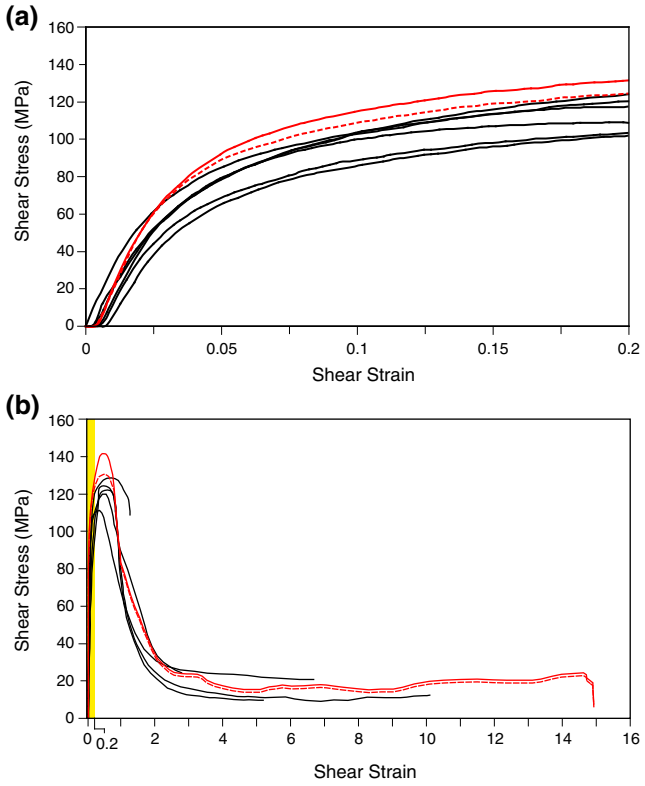

Figure 7. Shear strain (τ) versus shear strain (γ) plots of the torsion experiments. (a) The data sets were cropped ($\gamma = 0 - 0.2$, the yellow shaded area in Figure 7b) and expanded to show the mechanical behavior at low strains. (b) Full-scale ($\gamma = 0 - 15$) mechanical data showing a significant variation of shear stress against shear strain. In both Figures 7a and 7b the red curves represent $\gamma = 15$ experiment. The solid and stippled red curves are derived considering stress exponent (n) 5.13 and 43, respectively. All the other curves were calculated for $n = 5.13$.

shear strain at the outer boundary of the sample (the tangential plane of observation, Figure 3). Thus, a direct comparison of reaction kinetics between an x hour hydrostatic experiment and a deformation experiment of shear strain (γ) $\approx x$ is possible in terms of timescale. A summary plot of total melt and crystal content with continued deformation/time (Figure 6c) illustrates significant differences of melt and new crystal contents between hydrostatic and deformation experiments.

3.3. Mechanical Data

During an experimental run the data sets (pressure, temperature, torque, angular displacement, axial displacement, axial load, etc.) were recorded with respect to time. Measured torque (M) and angular displacement (θ) were used to calculate the shear stress (τ) and shear strain (γ) curves taking into account the sample geometry (length and diameter) and the iron jacket strength [*Paterson and Olgaard*, 2000]. For comparison with previous work, it is convenient to characterize the aggregate rheology using the power law stress exponent $n = (\partial \log \dot{\gamma} / \partial \log \tau) = 5.13$ while converting M to τ. We have noted that the stress exponent (n) does not remain constant with increasing shear strain, which is a point commented in the discussion of this paper; however, the magnitude of shear stress does not change significantly with changing stress exponent values. This is evident from the τ-γ plot of longest experiment (the solid and dotted red curves in Figures 7a and 7b). The mechanical data, viewed at finite shear strains ranging from $\gamma = 0.0$ to 0.2 in the τ-γ plot, initially displayed quasi-linear elastic behavior followed by a gradual transition to the plastic domain characterized by strain hardening (Figure 7a). The material yielded at low shear strain ($\gamma < 0.05$) at shear stress of ~60–65 MPa (Figure 7a). The large shear strain versus torque plot (Figure 7b) shows that strain hardening continued until peak shear stress was reached. The magnitudes of peak shear stress in different runs are not perfectly reproducible but vary in the range from $\tau \approx 110$ to 140 MPa at $\gamma \approx 0.8$–1.0. The curves followed a postpeak shear stress with an abrupt nearly linear strain weakening with ~60% shear stress drop until $\gamma = 2.0$–2.5. At that stage, flow stress is relatively

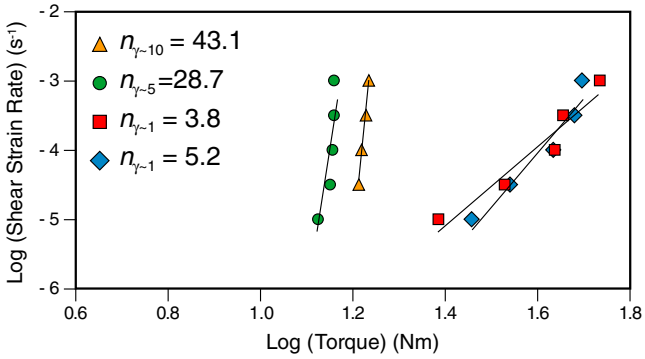

Figure 8. Logarithmic plot of measured torque (M) versus shear strain rate (γ) used to constrain the stress exponent (n), which was utilized to estimate the rheology of the deformed samples and to convert the measured torque (M) into shear stress (τ). The experiments were conducted after achieving three different finite strains ($\gamma = 1$, 5, and 10).

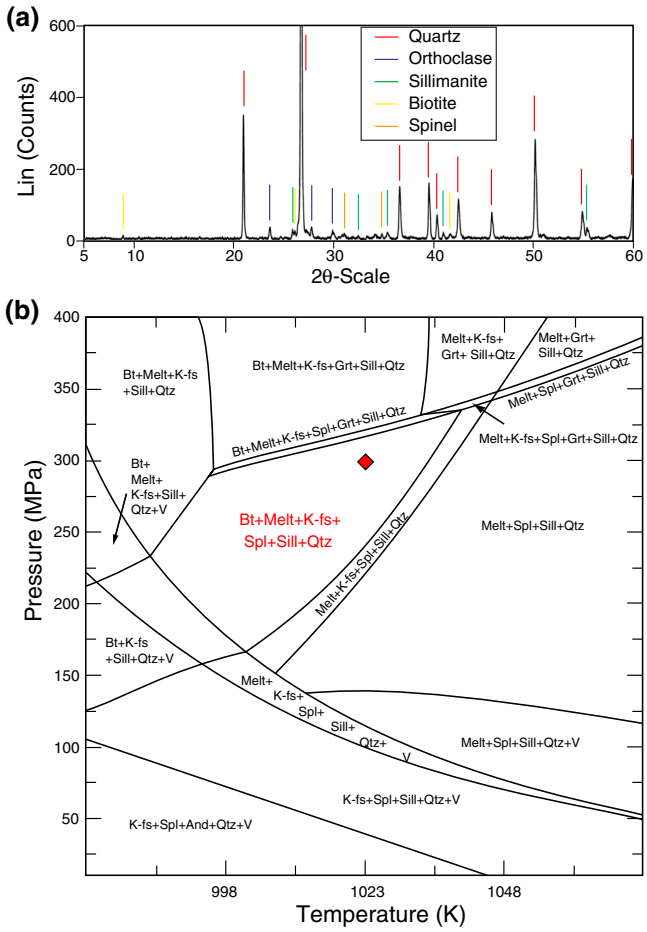

Figure 9. (a) XRD analysis of a deformed sample ($\gamma = 10$). The peak intensity distributions with respect to Figure 1b show that muscovite is absent during deformation while new peaks of biotite, K-feldspar, sillimanite, and spinel appeared as reaction products. (b) Calculated KFASH (K_2O–FeO–Al_2O_3–SiO_2–H_2O) phase diagram using Perple_X fed with the compositions of the starting materials. The red rhomb indicates the pressure-temperature (P-T) condition of the torsion experiments. The grid in that P-T field is represented with a composition which is similar to the composition obtained by XRD analysis in Figure 9a.

low (~ 10–20 MPa) and remains stable until $\gamma = 9$–10. In the longest experiment, strain hardening up to the shear stress value of 30 MPa occurred between $\gamma = 10$ and 15 and terminated when the torque finally dropped sharply due to sample failure.

To check the rheology of the deforming cylinder at its outer boundary, the stress exponent (n) was calculated by stepping strain rate (SSR) experiments at 750°C and 300 MPa with increasing or decreasing strain rate in a stepwise manner, when the torque (M) was nearly constant with progressive angular displacement (θ). Data were measured, at low ($\gamma \sim 1$), medium ($\gamma \sim 5$), and high ($\gamma \sim 10$) shear strains over a small strain interval of $\gamma < 0.5$–0.7. At low shear strain ($\gamma \sim 1$) n changes significantly with strain rate, from $n \sim 3$ at $\dot{\gamma} = 1 \times 10^{-5}\,s^{-1}$, increasing to $n \sim 10$–14 at $\dot{\gamma} = 1 \times 10^{-3}\,s^{-1}$. The average trend of stress exponent is calculated to be 3.8 to 5.2 (Figure 8). Data obtained from the medium and high shear strain experiment yield a more linear trend with $n = 28.7$ and 43.1, respectively (Figure 8).

4. Discussion

4.1. Mineral Reaction and Microstructure

SEM observation of the deformed samples suggests that there are complex interactions between microstructure and mineral reactions during progressive shearing. The generalized mineral reaction [*Thompson and Algor*, 1977; *Misra et al.*, 2009, 2011; *Tumarkina et al.*, 2011]

$$\text{Quartz} + \text{Muscovite} = \text{K-feldspar} + \text{Aluminosilicate (sillimanite)} + \text{Biotite} + \text{Spinel} + \text{melt}$$

was confirmed by XRD data (Figure 9a) and a theoretical phase diagram (Perple_X) [*Connolly*, 1990] (http://www.perplex.ethz.ch/) based on the composition of the starting quartz and muscovite (Figure 9b). Microstructures further suggest that the new minerals do not form simultaneously but sequentially, although it was not possible to detect the exact relative timing of the appearance of these new minerals. Partial melting and crystallization of biotite (and/or spinel) had started at $\gamma = 0.5$–1.0 and 2.0–3.0, respectively. Sillimanite and K-feldspar had both appeared at $\gamma = 3.0$–5.0. At $\gamma \sim 10$, all muscovite grains were consumed. The sample at $\gamma = 15$ contained almost no melt within the measurement error.

The microstructure development went hand in hand with mineral reactions and deformation. The initial fabric was completely replaced with a new evolving microstructure including microshear zones and reoriented old and newly crystallized minerals. The initial planar fabric aligned parallel to the shear direction; rotated antithetically; and showed microfolding, boudinage, and kinking [cf. *Misra and Burg*, 2012] of muscovite

grains (Figure 4a). Melt was restricted to tiny pockets on grain boundaries at $\gamma = 2$–3. Further shearing ($\gamma = 4$–7) caused connection of melt pockets (Figures 4c and 4d). At $\gamma = 5$–7 dehydration melting of muscovite sharply increased the melt content (15–20 area percent). As a result, grain boundaries were wetted and solid grains isolated from each other. This allowed melt segregation. At this stage, crystallization of new grains and rotated old quartz grains gave rise to S fabric and shear localization along shear bands, which were the avenues for sample-scale melt percolation [*Sawyer*, 1994; *Misra et al.*, 2009]. The new crystals within the shear bands, sillimanite, and biotite in particular, formed a "layering". A framework of new (mainly K-feldspar) and old (mainly quartz) crystals developed at $\gamma = 10$, where melt percentage started decreasing, and melt pockets became again separated. Production of partial melt probably stopped after total consumption of muscovite and removal of the source of water to trigger melting. At the highest shear strain ($\gamma = 15$) the melt had almost all disappeared and residual quartz and K-feldspar grains formed an interlocking texture of crystals.

In natural systems, partial melting followed by crystallization has been interpreted in terms of increase and then decrease of metamorphic pressure and temperature [*Brun and Martin*, 1978; *Sawyer and Robin*, 1986; *Jones and Brown*, 1990; *Barbey et al.*, 1990, 1995; *Kalt et al.*, 1999]. The experimental study presented here shows that the same phenomenon may happen at constant pressure-temperature conditions during progressive shearing. The individual crystals produced during the experiments were too small to measure their chemical compositions with a standard microprobe. However, the melting reactions, both under static and dynamic conditions, indicate that the system was not in equilibrium. The sample was confined, and neither solid nor liquid components had escaped from the sample assembly. However, an unknown amount of water was lost by diffusion through the iron jacket. We still consider that the experimental data have some relevance as it approximate natural systems where water is free to escape.

4.2. Rheology and Flow Law

The torsion experiments showed complex but reproducible shear stress (τ) versus shear strain (γ) relations that can be correlated with the microstructural and chemical evolution of the samples during progressive shear deformation. Based on the microstructures, crystal-melt ratio and calculated stress exponents (n) at different experimental stages, it is possible to divide the bulk rheology of the samples into four gradational domains (Figure 10)—(I) rheology during *solid state creep*, (II) rheology during *domination of partial melting*, (III) rheology during *simultaneous partial melting and crystallization*, and (IV) rheology during *domination of crystallization*. The initial stage (I) solid state creep, $\gamma < 1$, deformation is characterized by closure of porosity, rotation, kinking, and folding (Figure 4a) of muscovite grains [*Misra and Burg*, 2012]. The average range of stress exponent values ($n = 3.7$ to 5.1) suggests a strain rate sensitive power law rheology. The $\partial \log \dot{\gamma} / \partial \log \tau$ data (Figure 8) indicate that the strain rate sensitivity at low finite shear strain ($\gamma \sim 1$) ranges widely from $n = 3$ to 14, suggesting that the power law breakdown was already taking place at the fastest strain rate of $10^{-3}\ s^{-1}$. This typical nonlinear distribution of data in the $\partial \log \dot{\gamma} / \partial \log \tau$ plot has also been reported by other authors for the rheology of partially molten rocks [*Rutter and Neumann*, 1995, Figure 3b; *Zimmerman and Kohlstedt*, 2004, Figure 5]. This behavior may be explained by either a transition of creep mechanism [*Zimmerman and Kohlstedt*, 2004; *Misra et al.*, 2009] or increasing melt (fluid) in system. During solid state creep, grains remain in contact and can transmit stress to neighboring grains so that deformation is mainly matrix supported. With the increasing amount of melt, strain becomes partitioned between solid grains and melt [*Burg and Vigneresse*, 2002], which leads to shear localization and melt mobilization where the strain rate is faster [*Dell'Angelo and Tullis*, 1988]; this is accompanied by mechanical weakening of the bulk sample. During simultaneous crystallization and melting, new and old crystals in melt rarely interact due to higher melt-crystal ratio (Figures 6c and 10); they move and rotate freely with nearly no effect on the shear flow stress. At the domination of crystallization domain, when melting fraction starts to decrease because muscovite has been entirely consumed, the high stress exponent indicates that the rheology has very low sensitivity to strain rate. Grain interactions become more effective, which strain hardens the two-phase system (Figures 7 and 10). With further strain hardening the aggregate flow stress is greater than fracture stress and the sample becomes brittle.

The change of rheology from power law to exponential law or in other words strain rate sensitive to strain rate insensitive flow is known as Power Law Breakdown (PLB) [*Nabarro*, 1967; *Sherby and Burke*, 1968; *Sherby and Young*, 1975; *Pharr*, 1981; *Tsenn and Carter*, 1987]. The proposed mechanisms for PLB in literature include arbitrary and nonequilibrated clusters of point defects resulting in unusual vacancy generation and transition

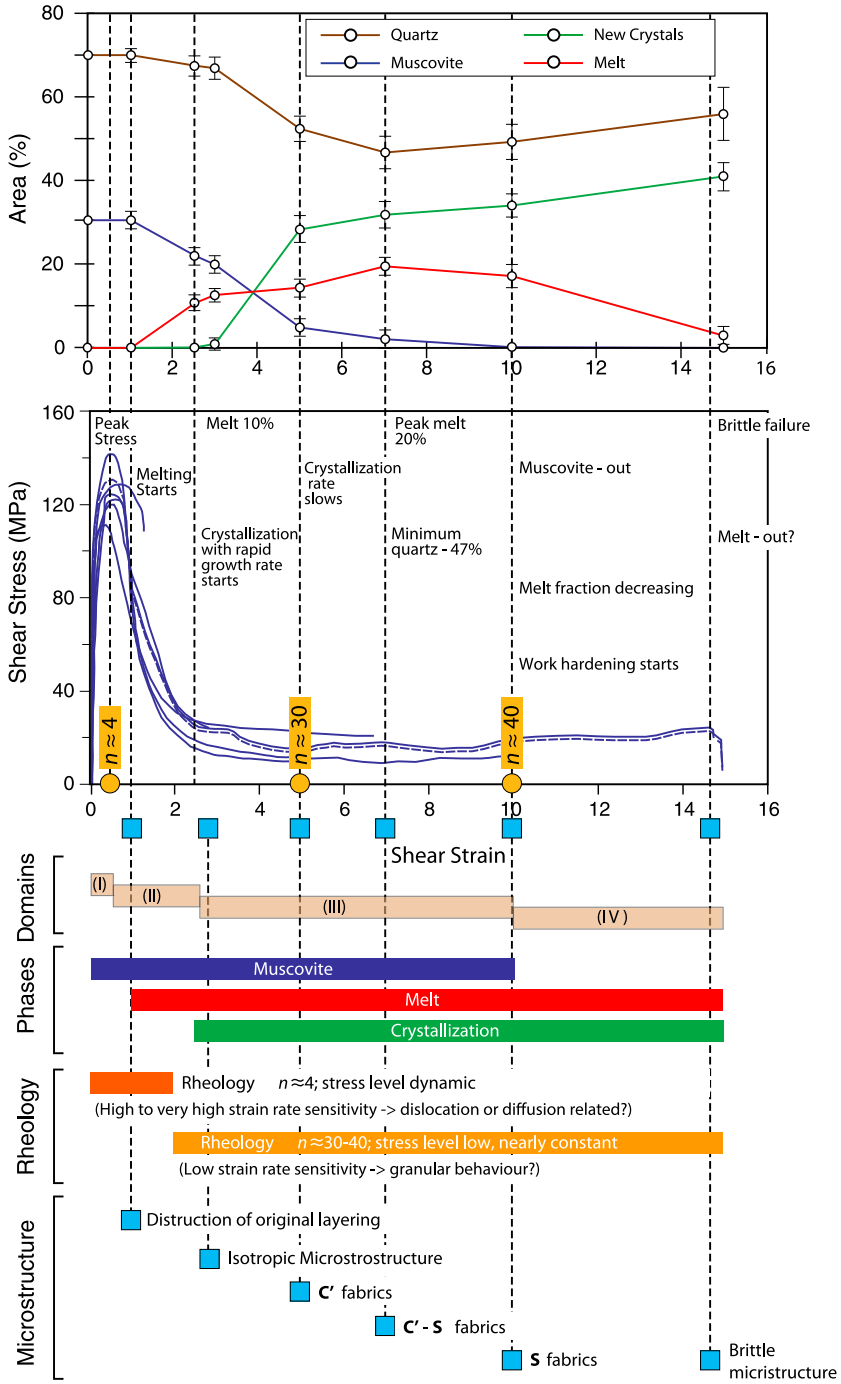

Figure 10. A review diagram summarizing and correlating the mechanical data, rheological domains, phase changes, and microstructures obtained from the experiments.

of microscale deformation mechanisms where the activation energy for creep has the same value as that of dislocation pipe diffusion [*Nabarro*, 1967; *Sherby and Weertman*, 1979]. Experiments on aluminum, polycrystalline galena, and clinopyroxenite [*Servi and Grant*, 1951; *Atkinson*, 1976; *Arieli and Mukherjee*, 1981; *Kirby and Kronenberg*, 1984] supported this consideration and showed the transition from diffusion-assisted dislocation motion to obstacle-limited dislocation glide. These driving forces of PLB are considered in these studies to be thermally activated energies that control dislocation mechanisms at lattice scale. However, the deformation of partially molten rocks at constant pressure-temperature conditions, as described in section 3,

apparently followed a different mechanism at a different scale to exhibit a rheological transition (strain rate sensitive ($1 < n < 7$) to strain rate insensitive ($n > 7$)), similar to PLB. We attribute the changing power exponents to the variations of melt and solid fractions and their mutual interactions coupled with evolution of shear-driven microstructures in the partially molten rock as discussed below.

The McClelland approximation [*McClelland*, 1961; *Langdon*, 1972] suggests that the presence of porosity will have an effect on the calculated shear stress and the stress exponent. The relationship is expressed as

$$\tau_{\text{eff}} = \frac{\tau_{\text{cal}}}{\left(1 - P^{\frac{2}{3}}\right)}$$

where P is the volume fraction of the porosity; τ_{eff} and τ_{cal} represent the effective and calculated shear stress, respectively. The aggregate at $\gamma \sim 1$ was devoid of melt, and the porosity was 1–2%. This suggests that pore spaces raise the effective stress value compared to the calculated ones by a factor of $\left(1 - P^{\frac{2}{3}}\right)^{-1}$. With porosity decreasing from 5% (initial material) to 2% (low-strain sample) the difference between τ_{eff} and τ_{cal} reduces from 15% to 7%. Clearly, a calculation of stress exponent with the τ_{eff} will yield a relatively lower value ($n = 5.0$ at 5% porosity), but the flow mechanism still remains in the strain rate sensitive domain, and the shear stress is at its maximum. An important observation at low shear strain in this study is the absence of localized deformation (e.g., shear bands). *Pan* [1983] argued by a linearized perturbation analysis that strain rate sensitivity (i.e., low-stress exponent, n) has the effect of retarding localization. This statement, based on theoretical analysis, is supported by our experimental observations that there is no localization of deformation at low shear strains with $n < 20$, whereas when $n > 20$ strain localization is evident with formation of C′, C′-S and S fabrics. Further deformation changes the original microstructure, porosity reduces to approximately 0%, and deformation localization occurs along narrow shear bands containing partial melt ($\gamma \sim 5$, $n \sim 30$). The mechanisms that reduce porosity are not clearly disclosed from microstructural observation. However, we assume that the pore spaces in the initial sample are in the drained condition. This assumption is based on the fact that we did not notice positive melt pressure (e.g., no melt is expelled from sample assembly), and the sample continued to flow without fracturing ($\gamma = 2$–10).

Strain rate sensitivity of a deforming polycrystalline aggregate is generally thought to be a function of applied strain rate, temperature, plastic strain, and microstructure. In our experiments, applied strain rate and temperature were kept constant. Therefore, the increasing stress exponent, n, should reflect plastic strain and the subsequent microstructural evolution. A series of localization microstructures (C′, C′-S, S fabrics, and open fractures) was observed with progressive deformation at relatively low and constant shear stress. Deformation localization at nearly constant flow stress and in adiabatic conditions may result from strain partitioning by concentration of plastic strain in the shear bands and less plastic or elastic strain in the matrix [*Needleman*, 1988]. Had the matrix outside the narrow shear bands been deforming plastically, the bulk sample would then be expected to flow homogeneously with no shear band formation. In the experiments reported here the material was at the same time undergoing extensive mineralogical changes. The relatively low magnitude of flow stress is probably due to low melt pressure in the shear bands. After muscovite out reaction is completed (at $\gamma = 10$), the shear bands cannot accommodate further plastic strain as the reaction producing the melt no longer operates. The potential for shear localization is thus reduced and the sample microstructure becomes increasingly homogeneous (for comparison, see Figures 4d and 4e). The sample at this stage may be considered as having a "new" microstructure consisting of very fine grain polycrystalline aggregate with 10–15% melt. Further deformation requires work hardening in response to decreasing melt content. The small, but increasing flow stress after $\gamma = 10$ is the response to progressive straining of the matrix, which at $\gamma = 15$ failed by producing shear fractures.

4.3. Geological Implications

Under hydrostatic condition, the high viscosity of silicic melt [*Rutter and Neumann*, 1995] and its low volume retard the potential of gravity-driven porous flow to segregate melt. Extraction of granitic melt from its source is promoted by local pressure gradients due to deformation. Applying our experimental results to natural systems, we propose that deformation influences melt movement in two ways. First, it increases the melt volume relative to that of hydrostatic state by accelerating the phyllosilicate-dehydration reaction. The relatively large volume of melt assists density separation between melt and solid crystals allowing the gravity-driven

porous flow to operate. Second, the formation of shear bands and their network provides pathways for melt distribution. The melt migration through the proposed mechanism is not directly observed in experiments, which were a mechanically close system. However, this hypothesis is likely to be valid in natural, opened systems.

Most of the previous studies [e.g., *Rushmer*, 1995; *Misra et al.*, 2009] have argued a brittle behavior at the onset of deformation, which reduces the grain size and increases reaction kinetics. The presence of melt likely activates strain partitioning [*Vigneresse and Tikoff*, 1999], which promotes and propagates as crustal-scale weak zones as detachment planes [*Misra et al.*, 2011]. Development of several shear-induced fabrics in the experiments presented in this study, particularly at the stage of simultaneous partial melting and crystallization, supports this idea. Furthermore, our starting material is analogous to phyllosilicate-bearing sediments, dragged from the accretionary wedge along a subducting interface. The experimental setting resembles small but important segment of sediment-fed channel along the subduction interface documenting the onset of dehydration-triggered partial melting, total consumption of the dehydrating minerals at the expense of melting, and nucleation of new crystals.

The increase of the stress exponent (n) from $n \sim 1$ (diffusion creep) to n ~3–5 (dislocation creep) and higher values (Figure 8) has implications on the bulk rheology of partially molten pelites and should be taken into consideration for geodynamic modeling that includes syntectonic partial melting. Indeed a pseudo viscosity, or effective viscosity (η_{eff}), may be estimated as the ratio of strain rate ($\dot{\gamma}$) to shear stress (τ). This can be represented as $\eta_{\text{eff}} = \frac{\tau}{A\tau^n}$, where A is the material constant in power law rheology. It therefore scales as τ^{1-n} (with $n > 1$). Since n increases with shear strain in the present case, the effective viscosity decreases accordingly, resulting in strain softening. It corresponds to the Herschel-Bulkley equation type, generally accepted for that category of material: $\tau = K\dot{\gamma}_n$, where K is a constant of proportionality and the exponent n is generally <1, corresponding to shear thinning.

5. Conclusion

A synthetic mixture of quartz and muscovite taken as analogue to pelitic rock of controlled grain size, composition, microstructure, and physical properties was prepared to deform in a series of torsion experiments at constant pressure, temperature, and deformation rate. The material showed a complex evolution of microstructures and mechanical properties, closely integrated with syndeformation partial melting and crystallization of neoblasts. The large strain noncoaxial nature of deformation resembles natural shear deformation of rocks.

The principal outcomes of this study are the following:

1. Deformation plays an important role in governing the reaction kinetics of a metapelitic composition. The rate of muscovite dehydration is significantly faster under deformation, producing larger volume of partial melt relative to hydrostatic conditions. The rate of melt production is a function of finite strain, given the other extrinsic parameters.
2. A dramatic weakening of rock strength is noted at the onset of partial melting. The weakening is also associated with heterogeneous flow and strain partitioning defined by shear localizations of various orientations. The localized deformation bands are often characterized by segregated partial melt-filled channels and oriented neoblasts.
3. Successive percolation thresholds in the sense of *Vigneresse et al.* [1996] were experimentally demonstrated. The percolations thresholds are associated with first strain rate sensitive and then rate insensitive flow mechanisms characterized by high and low shear stress, respectively. The changing strain rate sensitivity results from melt-crystal ratio and their mutual interactions coupled with the evolution of shear-driven localization microstructures.
4. This novel experimental approach documents a coupling of differential stress- and reaction-driven partial melting and crystallization applicable to understand the dynamics of crustal rocks. We have established that deformation is one of the essential parameters in driving relatively viscous silicic melt to segregate and migrate from the source.
5. After the completion of melt migration due to less or no melt production, the source rock tends to retain its strength. Consequently, strain rate insensitive flow becomes dominating deformation mechanism. Further straining may lead to embrittlement of the rock due to the formation of shear fractures.

Acknowledgments
Robert Hofmann and Karsten Kunze are acknowledged for the technical assistance in the laboratory and SEM work, respectively. Christian Mensing conducted the TG analysis of muscovite. Helpful discussions and suggestions from Elizaveta Tumarkina, James Connolly, Yury Podladchikov, and Ernie Rutter at the different stages of the work improved the content of the manuscript. Constructive comments from two anonymous reviewers significantly improved the quality of the manuscript. This work is a part of SNF project (2-77113-07).

References

Arieli, A., and A. K. Mukherjee (1981), On the power-law breakdown during high temperature creep of FCC metals, in *Creep and Fracture of Engineering Materials and Structures*, edited by B. Wilshire and D. R. J. Owen, pp. 97–111, Pineridge Press, Swansea, U. K.

Arzi, A. A. (1978), Critical phenomena in rheology of partially molten rocks, *Tectonophysics*, *44*, 173–184.

Atkinson, B. K. (1976), The temperature- and strain rate-dependent mechanical behavior of a polycrystalline galena ore, *Econ. Geol.*, *71*, 513–525.

Barbey, P., J. Macaudière, and J. P. Nzenti (1990), High-pressure dehydration melting of metapclites. Evidence from the migmatites of Yaounde (Cameroon), *J. Petrol.*, *31*, 401–427.

Barbey, P., P. Allouc, M. Brouand, and F. Albarède (1995), Rare earth patterns in zircons from the Manaslu granite and Tibetan slab migmatites (Himalaya): Insights in the origin and evolution of a crustally-derived granite magma, *Chem. Geol.*, *125*, 1–17.

Barboza, S. A., and G. W. Bergantz (1998), Rheological transitions and the progress of melting of crustal rocks, *Earth Planet. Sci. Lett.*, *158*, 19–29.

Berthé, D., P. Choukroune, and P. Jégouzo (1979), Orthogneiss, mylonite and non coaxial deformation of granites: The example of the South Armorican Shear Zone, *J. Struct. Geol.*, *1*, 31–42.

Brown, M. (1994), The generation, segregation, ascent and emplacement of granite magma: The migmatite-to-crustally-derived granite connection in thickened orogens, *Earth Sci. Rev.*, *36*, 830–130.

Brown, M. (2007), Crustal melting and melt extraction, ascent and emplacement in orogens: Mechanisms and consequences, *J. Geol. Soc. London*, *164*, 709–730.

Brown, M., and G. S. Solar (1997), Shear-zone systems and melts: Feedback relations and self organization in orogenic belts, *J. Struct. Geol.*, *20*, 211–227.

Brun, J. P., and H. Martin (1978), Relations métamorphisme-déformation au cours de l'évolution dynamique d'un dome migmatitique: Le massif de Saint Malo (France), *Bull. Soc. Géol. Fr.*, *20*, 91–101.

Burg, J.-P., and J. L. Vigneresse (2002), Non-linear feedback loops in the rheology of cooling-crystallizing felsic magma and heating-melting felsic rock, in *Deformation Mechanisms, Rheology and Tectonics: Current and Future Perspectives*, Sp. Pub., vol. 200, edited by S. De Meer et al., pp. 275–292, G.M. Geol. Soc., London, U. K.

Carter, N. L., and M. C. Tsenn (1987), Flow properties of continental lithosphere, *Tectonophysics*, *136*, 27–63.

Clemens, J. D., and D. Vielzeuf (1987), Constraints on melting and magma production in the crust, *Earth Planet. Sci. Lett.*, *86*, 287–306.

Connolly, J. A. D. (1990), Multivariable phase diagrams: An algorithm based on generalized thermodynamics, *Am. J. Sci.*, *290*, 666–718.

Dell'Angelo, L. N., and J. Tullis (1988), Experimental deformation of partially melted granitic aggregates, *J. Metamorph. Geol.*, *6*, 495–615.

Einstein, A. (1906), Eine neue Bestimmung der Molekul-dimensionen, *Ann. Phys.*, *19*, 289–306.

Jinescu, V. V. (1974), The rheology of suspensions, *Int. Chem. Eng.*, *14*, 397–420.

Jones, K. A., and M. Brown (1990), High-temperature "clockwise" PT paths and melting in the development of regional migmatites: An example from southern Brittany, France, *J. Metamorph. Geol.*, *8*, 551–578.

Kalt, A., A. Berger, and P. Blümel (1999), Metamorphic evolution of cordierite bearing migmatites of the Bayerische Wald (Variscan belt, Germany), *J. Petrol.*, *40*, 601–627.

Kirby, S. H., and A. K. Kronenberg (1984), Deformation of clinopyroxenite: Evidence for a transition in flow mechanisms and semibrittle behavior, *J. Geophys. Res.*, *89*, 3177–3192, doi:10.1029/JB089iB05p03177.

Lambert, I. B., J. K. Robertson, and P. J. Wyllie (1969), Melting reactions in the system $KAlSi_3O_8$-SiO_2-H_2O to 18.5 kilobars, *Am. J. Sci.*, *267*, 609–626.

Langdon, T. G. (1972), Dependence of creep rate on porosity, *J. Am. Ceram. Soc.*, *55*, 630–631.

McClelland, J. D. (1961), Plastic flow model of hot-pressing, *J. Am. Ceram. Soc.*, *44*, 526.

Misra, S., and J.-P. Burg (2012), Mechanics of kink-bands during torsion deformation of muscovite aggregate, *Tectonophysics*, *548–549*, 22–33.

Misra, S., L. Burlini, and J.-P. Burg (2009), Strain localization and melt segregation in deforming metapelites, *Phys. Earth Planet. Int.*, *117*, 173–179.

Misra, S., J.-P. Burg, and D. Mainprice (2011), Effect of finite deformation and deformation rate on partial melting and crystallization in metapelites, *J. Geophys. Res.*, *116*, B02205, doi:10.1029/2010JB007865.

Nabarro, F. R. N. (1967), Steady-state diffusional creep, *Philos. Mag.*, *16*, 231–237.

Needleman, A. (1988), Material rate dependence and mesh sensitivity in localization problems, *Comput. Methods Appl. Mech. Eng.*, *67*, 69–85.

Pan, J. (1983), Perturbation analysis of shear strain localization in rate sensitive materials, *Int. J. Solids Struct.*, *19*, 153–164.

Paterson, M. S., and D. L. Olgaard (2000), Rock deformation tests to large shear strains in torsion, *J. Struct. Geol.*, *22*, 1341–1358.

Pharr, G. M. (1981), Some observations on the relation between dislocation substructure and power law breakdown in creep, *Scripta Metall.*, *15*, 713–717.

Ramsay, J. G. (1980), Shear zone geometry: A review, *J. Struct. Geol.*, *2*, 83–99.

Renner, J., B. Evans, and G. Hirth (2000), On the rheological critical melt percentage, *Earth Planet. Sci. Lett.*, *181*, 585–594.

Roscoe, R. (1952), The viscosity of suspensions of rigid spheres, *Br. J. Appl. Phys.*, *3*, 267–269.

Rushmer, T. (1995), An experimental deformation study of partially molten amphibolite: Application to low-melt fraction segregation, *J. Geophys. Res.*, *100*, 15,681–15, 695, doi:10.1029/95JB00077.

Rutter, E. H., and D. H. K. Neumann (1995), Experimental deformation of partially molten westerly granite under fluid-absent conditions, with implications for the extraction of granitic magmas, *J. Geophys. Res.*, *100*(B8), 15,697–15,715, doi:10.1029/94JB03388.

Rutter, E. H., K. H. Brodie, and D. H. Irving (2006), Flow of synthetic, wet, partially molten "granite" under undrained conditions: An experimental study, *J. Geophys. Res.*, *111*, B06407, doi:10.1029/2005JB004257.

Sawyer, E. D. (1987), The role of partical melting and fractional crystallization in determining discordant migmatite leucosome compositions, *J. Petrol.*, *28*, 445–473.

Sawyer, E. W. (1994), Melt segregation in the continental crust, *Geology*, *22*, 1019–1022.

Sawyer, E. W., and P. Y. F. Robin (1986), The subsolidus segregation of layer-parallel quartz—Feldspar veins in greenschist to upper amphibolite facies metasediments, *J. Metamorph. Geol.*, *4*, 237–260.

Servi, I. S., and N. J. Grant (1951), Creep and stress rupture behavior of aluminum as a function of purity, *Trans. AIME*, *191*, 909–916.

Sherby, O. D. (1962), Factors affecting the high temperature strength of polycrystalline solids, *Acta Metall.*, *10*, 135–147.

Sherby, O. D., and P. M. Burke (1968), Mechanical behavior of crystalline solids at elevated temperature, *Prog. Mater Sci.*, *13*, 325–390.

Sherby, O. D., and J. Weertman (1979), Diffusion-controlled creep: A dislocation, *Acta Metall.*, *27*, 387–400.

Sherby, O. D., and C. M. Young (1975), Some factors influencing the strain rate-temperature dependence of the flow stress in polycrystaliine solids, in *Rate Processes in Plastic Deformation of Materials*, edited by J. C. M. Li and A. K. Mukherjee, pp. 497–541, ASM, Metals Park, Ohio.

Sherby, O. D., R. L. Orr, and J. E. Dorn (1954), Creep correlations of metals at elevated temperatures, *Trans. AIME*, *200*, 71–80.

Stauffer, D. (1985), *Introduction to Percolation Theory*, 124 pp., Taylor and Francis, London, U. K.

Thompson, A. B. (1982), Dehydration melting of pelitic rocks and the generation of H_2O-undersaturated granitic liquids, *Am. J. Sci.*, *282*, 1567–1595.

Thompson, A. B., and J. R. Algor (1977), Model systems for anatexis of pelitic rocks: I. Theory of melting reactions in the system $KAlO_2$–$NaAlO_2$–Al_2O_3–SiO_2–H_2O, *Contrib. Mineral. Petrol.*, *63*, 247–269.

Tsenn, M. C., and N. L. Carter (1987), Upper limit of power law creep of rocks, *Tectonophysics*, *136*, 1–26.

Tumarkina, E., S. Misra, L. Burlini, and J. A. D. Connolly (2011), An experimental study of the role of shear deformation on partial melting of a synthetic metapelite, *Tectonophysics*, *503*, 92–99.

Van der Molen, I., and M. S. Paterson (1979), Experimental deformation of partially melted granite, *Contrib. Mineral. Petrol.*, *98*, 299–318.

Vielzeuf, D., and J. R. Holloway (1988), Experimental determination of the fluid-absent melting reactions in the politic system: Consequences for crustal deformation, *Contrib. Mineral. Petrol.*, *98*, 257–276.

Vigneresse, J. L., and B. Tikoff (1999), Strain partitioning during partial melting and crystallizing felsic magmas, *Tectonophysics*, *312*, 117–132.

Vigneresse, J. L., P. Barbey, and M. Cuney (1996), Rheological transitions during partial melting and crystallization with application to felsic magma segregation and transfer, *J. Petrol.*, *37*, 1579–1600.

Zimmerman, M. E., and D. Kohlstedt (2004), Rheological properties of partially molten Lherzolite, *J. Petrol.*, *45*, 275–298.